ORIGINAL ARTICLE

Repair of aluminum 6061 plate by additive friction stir deposition

L. Peter Martin [1,2] (iD) · Allen Luccitti [2] · Mark Walluk [2]

Abstract

The deposition of new alloy to replace a worn or damaged surface layer is a common strategy for repairing or remanufacturing structural components. For high-performance aluminum alloys common in the automotive, aerospace, and defense industries, however, traditional fusion-based deposition methods can lead to solidification cracking, void formation, and loss of strength in the heat-affected zone. Solid-state methods, such as additive friction stir deposition (AFSD), mitigate these challenges by depositing material at temperatures below the melting point. In this work, a solid-state volumetric repair was performed using AFSD of aluminum alloy 6061-T6 to fill grooves machined into the surface of a plate of 6061-T651. The groove-filling process is relevant to replacement of cracked or corroded material after removal by localized grinding. Three groove geometries were evaluated by means of metallographic inspection, tensile testing, and fatigue testing. For the process conditions and groove geometries used in this study, effective mixing of the substrate and deposited alloy were achieved to a depth of 3.1–3.5 mm. Below that depth, the interface between the substrate and AFSD alloy exhibited poor bonding associated with insufficient shear deformation. This suggests a practical limitation of approximately 3 mm for the depth of repair by groove filling using the current combination of process parameters, materials, and tool design. The mechanical properties of the filler alloy, the depth of the heat-affected zone, and areas for further optimization are discussed within the context of precipitation hardened aluminum alloys.

Keywords Additive friction stir deposition · AFSD; 6061-T6 · Repair

1 Introduction

Repairs in lightweight structural alloys have historically been based on fusion processes, such as gas tungsten arc welding or tungsten inert gas welding [1, 2]. In many aluminum and magnesium alloys, these methods are prone to fusion-related defects, including porosity, cracking, inclusions, undesirable columnar microstructures, and phase segregation, that can severely degrade the mechanical properties [3]. In addition, even in the "weldable" alloys, such as aluminum 6061, thermal effects from the fusion process lead to loss of strength in the heat-affected zone (HAZ). As a result, solid-state processes based on fiction stir technologies have been gaining increasing attention for repair applications [3, 4].

Friction stir welding (FSW) is a solid-state joining method that avoids many of the problems associated with fusion processes [5]. In FSW, a rotating, non-consumable "pin" is plunged into the joint between two solid workpieces, then traversed along the joint line. Heat generated by friction plasticizes the material around the pin, and the rotation of the pin transfers the plasticized material from the leading edge to the trailing edge. The resultant weld is formed by solid-state mixing, and the high strains and comparatively low temperatures (typically $0.6–0.9 T_{melt}$) associated with the process yield refined microstructures and improved mechanical properties associated with dynamic recrystallization [6]. FSW is widely accepted to provide several benefits over traditional fusion welding, including favorable microstructures; however, FSW suffers from the limitation that it only re-locates the substrate material, and provides no capacity to add material to fill cracks, gouges or holes.

Since the late 1990s, several related technologies have been developed to extend the beneficial microstructural effects of FSW to additive material applications [7–9]. One of these

✉ L. Peter Martin
   lpmgis@rit.edu

1   Rochester Institute of Technology, Sustainability Institute Hall
    81-2161, 190 Lomb Memorial Drive, Rochester, NY 14623, USA

2   Golisano Institute for Sustainability, Rochester Institute of
    Technology, Rochester, NY, USA

methods, additive friction stir deposition (AFSD), has the potential to enable high deposition rates (>1000 cm³/h) during the manufacture of moderately complex geometries [10, 11]. Known commercially as MELD [12, 13], AFSD utilizes a hollow, rotating tool through which the feed material is delivered in the form of a powder or solid rod [14]. The rotation of the tool generates heat through friction at the interfaces between the filler, substrate, and tool [8, 15]. The filler material bonds with the substrate through plastic deformation, and is deposited as a single layer as the tool is traversed across the surface, Fig. 1. 3D parts can be fabricated by selectively adding subsequent layers, and the resultant components have been reported to exhibit fine, equiaxed microstructures with enhanced wear, corrosion, and mechanical properties [7–9, 16]. While the first reported applications of AFSD were for additive manufacturing of aluminum and magnesium alloys [17, 18], additional results have been reported for Inconel 625 [12, 19], Ti-6Al-4V [20], copper [21], and aluminum-matrix composites [13].

AFSD has obvious potential for repair applications; however, only two publications were identified that directly assess implementation strategies [3, 22]. Griffiths et al. evaluated AFSD for hole and groove filling in of 7075 aluminum plate, and reported complete filling of the features combined with extensive feed/substrate mixing and good bonding in the upper portions of the repair. They also reported poor repair quality in the lower (deeper) portions of the features, with evidence of insufficient shear mixing at depths exceeding 1.3–1.7 mm below the original surface [22]. Finally, they observed up to 15% decrease in the hardness of the repaired volume relative to the original feed material, and attributed this change to the dissolution of the hardening precipitates (e.g., loss of temper). Qi et al. evaluated a radial method to reduce the diameter of tolerance-exceeding holes in AZ31 magnesium alloy plate [3]. It should be noted that the repair material comprised plugs pre-inserted into the holes, and was not actively fed into the interface; thus, the method is not strictly relevant to the AFSD discussion. Nevertheless, they observed distinct microstructures associated with the stir zone (SZ),

thermomechanical affected zone (TMAZ), HAZ, and base metal (BM), and documented an inverse correlation between hardness and the grain size associated with the different regions. Finally, they measured the tensile strength and compressive shear strength to be 94% and 75%, respectively, of the as-manufactured plate.

The present study evaluates repair strategies using 6061-T6 feedstock to fill grooves in a plate of aluminum alloy 6061-T651. Alloy 6061 is a medium-strength, heat treatable Al–Mg–Si with excellent formability and good corrosion resistance, and it is one of the most widely used alloys in the 6XXX series [23, 24]. The major solutes, Mg and Si, provide strength by precipitation hardening associated with metastable phases that precede the formation of the stable Mg_2Si β-phase [23, 25, 26]. The repair strategy, which was similar to that reported by Griffiths et al. [22], simulates replacement of cracked or corroded material after removal by localized grinding. Three crack geometries were investigated, "V"-shaped, radiused (hemi-cylindrical), and square. The 6061-T6 filler was deposited by AFSD using process parameters that were informed by prior research, and the resultant repairs were analyzed by metallography, microhardness, tensile and fatigue testing, and fractography. The goal was to explore the practical benefits and limitations of AFSD 6061 as an additive repair for age-hardened aluminum alloys.

2 Materials and experimental procedures

2.1 Materials

The substrate material was a 12.7-mm-thick plate of aluminum alloy 6061-T651, and the feedstock (filler) material was a 9.4 mm × 9.4 mm square bar of alloy 6061-T6. Table 1 provides the chemical composition of the plate as determined by laser induced breakdown spectroscopy (SciAps Z-200 Handheld LIBS Analyzer), along with the ASTM specification for the alloy [27]. The specified Young's modulus, 0.2%

Fig. 1 a Schematic of the AFSD process, showing the rotating tool, feedstock, and deposited layer; b cross-sectional view illustrating the groove-filling process, and indicating frictional heating and extrusion of the feedstock
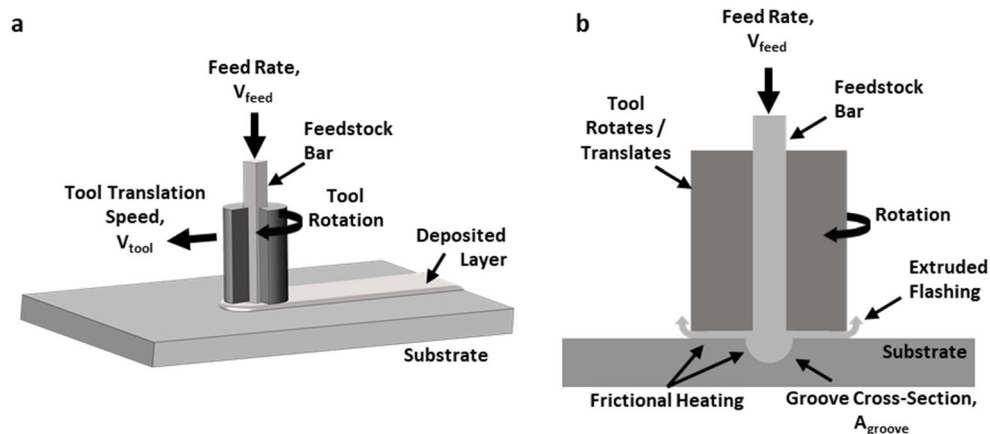
Table 1 Chemical composition, in weight percent, of the 6061 plate as determined by laser induced breakdown spectroscopy (LIBS). Also provided is the ASTM-specified composition

Element	6061 LIBS	6061[a] ASTM B209M-14
Si	0.56	0.40–0.80
Fe	0.49	0.7
Cu	0.18	0.15–0.40
Mn	0.06	0.15
Mg	0.82	0.80–1.2
Cr	0.07	0.04–0.35
Zn	0.04	0.25
Ti	0.03	0.15
Other-total	0.029	0.15
Al	Remainder	Remainder

[a] Values are maxima unless given as a range

offset yield strength, and tensile strength are also tabulated in Table 2. As indicated in the table, these values were obtained from ASTM B209M and the relevant product datasheets [27]. The 450 mm × 305 mm substrate plate was prepared for AFSD by machining surface grooves with the different geometries shown in Fig. 1. The three geometries were designated as "V" for the truncated triangle (left), "R" for the hemi-cylindrical radius (middle), and "S" for the square shape (right). The V and S grooves were 6.4 mm wide, while the R grooves were 12.7 mm wide, and all grooves were 6.35 mm in depth.

2.2 AFSD process

Additive friction stir deposition (AFSD) was performed by MELD Manufacturing Corporation (Christiansburg, VA, USA) on a MELD B8 system with a 38-mm tool head. A square bar of Alloy 6061-T6 with chamfered corners was used as the filler material (feedstock). The square profile of the feedstock facilitates transfer of torque from the tool to the feedstock, allowing the feedstock to rotate with the tool. The bottom surface of the tool head was flat except for four small protrusions (height ~1.5 mm) to promote vertical mixing

between the deposited material and the substrate. The protrusions comprised two orthogonal pairs arranged around the central square feedstock at radial positions of ~9.0 mm and 14.0 mm. Table 3 shows the process parameters used for the 1st pass over each groove. The process parameters were designed to fill the groove on the 1st pass by scaling the tool translation speed V_{tool} and feedstock feed rate V_{feed} to provide a deposition rate R_{dep} (mm³/s) equal to approximately 2.8×–3.6× the volume of the groove and substrate-tool gap transited by the tool each second, $R_{groove} + R_{layer}$ (also mm³/s), where the excess material was applied to ensure complete filling of the grooves and to increase the pressure below the tool in order to maximize shearing of the substrate. The process parameters are interrelated via the relationships:

$$R_{dep}\left[\frac{mm^3}{s}\right] = A_{\text{feed}}\left[mm^2\right] \cdot V_{\text{feed}}\left[\frac{mm}{s}\right] \tag{1}$$

$$R_{groove}\left[\frac{mm^3}{s}\right] = A_{\text{groove}}\left[mm^2\right] \cdot V_{\text{tool}}\left[\frac{mm}{s}\right] \tag{2}$$

$$R_{layer}\left[\frac{mm^3}{s}\right] = W_{\text{tool}}[mm] \cdot z_{\text{step}}[mm] \cdot V_{\text{tool}}\left[\frac{mm}{s}\right] \tag{3}$$

where A_{feed} and A_{groove} are the cross-sectional areas of the feedstock and the groove, respectively, W_{tool} is the width (diameter) of the tool, and z_{step} is the nominal layer thickness as determined by the increment in the z-coordinate of the tool between passes. Note that for the 1st, filling pass, the base of the tool was set to a height approximately 0.5 mm above the surface of the substrate.

Process parameters for subsequent cover passes were adjusted by the operator in real time to optimize the process performance, in particular the formation of flashing caused by excessive extrusion of material from between the tool and substrate. The relevant parameters are the tool rotation rate ω (RPM), V_{feed} (mm/s), V_{tool} (mm/s), and the interpass z_{step} (mm). These parameters determine the dependent parameters of heat input (via friction and material plasticity), force on the feedstock, and volumetric deposition rate. Some trial and error was employed during the 2nd passes in order to determine the optimal parameters, which resulted in slight process variability (Table 4). Figure 3 shows the final result, where the V, R,

Table 2 Expected mechanical properties of 6061-T6/T651, the as-received condition of the plate and filler feedstock. Also shown for reference are the properties of naturally aged and annealed 6061 (6061-T4 and 6061-O, respectively). All values are from ASTM B209M-14 unless noted otherwise

Material	Young's modulus[a], GPa	Yield strength, MPa	Tensile strength, MPa	Elongation, %	Vickers hardness[a]
6061-T651/T6	68.9	240	290	8	107
6061-T4	68.9	110	205	16	74
6061-O	68.9	85	150	18	-

[a] From product datasheet

Table 3 AFSD parameters for fill passes

Groove geometry	V	R	S
Groove cross section, A_{groove} [mm^2]	21.3	63.3	40.3
Tool rotation rate, ω [RPM]	325	325	325
Feedstock feed rate, V_{feed} [mm/s]	2.1	3.4	2.5
Tool translation speed, V_{tool} [mm/s]	1.3	1.3	1.3
Layer thickness, z_{step} [mm]	0.5	0.5	0.5
Layer cross section, $W_{tool} \cdot z_{step}$ [mm^2]	19.5	19.5	19.5
Deposition rate, R_{dep} [mm^3/s]	185.1	296.0	221.8
Volume of groove at traverse rate, R_{groove} [mm^3/s]	27.1	80.4	51.2
Volume of layer at traverse rate, R_{layer} [mm^3/s]	24.8	24.8	24.8
Fill volume, $R_{groove} + R_{layer}$ [mm^3/s]	51.8	105.2	75.9
Fill ratio, $R_{dep}/(R_{groove} + R_{layer})$	3.6	2.8	2.9

and S grooves are shown from left to right after filling followed by one (V and S) or three (R) cover passes to homogenize the surface. The two additional cover passes, as well as the decreased z_{step} of 0.5 mm in the first cover pass, were applied to the R groove in order to facilitate mixing at the interface. This was done in order to compensate for the wider geometry of the R groove (12.7 mm) relative to the V and S grooves (6.7 mm), and the resultant loss of constraint of the filler material.

2.3 Metallography and microhardness testing

Metallographic samples were sectioned from several locations in the AFSD-filled grooves. These sections were mounted in a room temperature curing acrylic potting material, polished, and etched for inspection by light optical microscopy (LOM). Polishing was performed by sequentially grinding to a 600 grit SiC paper, then polishing with 9-, 3-, and 1-μm diamond suspensions, and final polishing with 0.05 μm colloidal silica. Etching was performed by immersion for 30 s in a 10% solution of NaOH at 60 °C. Microstructures were imaged using an Olympus IX-50 inverted metallurgical

microscope. Vickers microhardness depth profiles were measured at three locations on the metallographic cross sections: in the center of the AFSD feature, and at approximately the quarter-width locations on either side. The testing used a 200 g load and a 13-s dwell time, and was performed using a LECO LM-248 AT microhardness tester.

2.4 Tensile and fatigue testing

Tensile and fatigue testing used a 100 kN load cell on an Instron 8801 servo-hydraulic fatigue testing system. The tensile testing was performed in accordance with ASTM B557-15 [28] using a constant crosshead speed of 0.085 mm/s (5.08 mm/min). Test samples were extracted from selected locations in each AFSD-filled groove, and were sectioned from the top 6.35 mm of the substrates so that the central portion of the gauge was comprised of AFSD material and excluded the underlying substrate alloy. The specimen geometry was derived from the guidelines provided by ASTM B557 for rectangular sub-sized specimens [28], except that the grip ends were shortened to accommodate the spacing of the AFSD repairs on the substrates. Strain measurements below 2% were made with an Instron 2620-series dynamic axial clip-on strain gauge extensometer using a 12.5-mm gauge length. The tests were paused at 2% strain in order to remove the extensometer, and strains >2% were estimated from the crosshead displacement. The values for Young's modulus were calculated from the initial slopes of the stress vs. strain curves, the yield strengths were calculated at a 0.2% offset using the same slopes, and the tensile strengths were determined from the maximum stresses attained in the curves. The elongation at fracture was determined from the value of the strain when the load fell below 10% of the maximum [28]. Fatigue testing used load-controlled, completely reversed cycling ($R = -1$) at 15 Hz. The fatigue specimen geometry was based on the continuous radius geometry found in ASTM E466 [29], and the surfaces were finished by lightly sanding to 400 grit (44 μm). Figure 4 shows the geometry of the tensile and fatigue

Table 4 AFSD parameters for cover passes

Layer number	2			3	4
Groove geometry	V	R	S	R	R
Tool rotation rate, ω [RPM]	325	325	325	325	325
Feedstock feed rate, V_{feed} [mm/s]	2.1	1.3	2.5	2.5	2.5
Tool translation speed, V_{tool} [mm/s]	2.8	3.4	2.1	3.4	2.5
Layer thickness, z_{step} [mm]	1.0	0.5	1.0	1.0	1.0
Layer cross section, $W_{tool} \cdot z_{step}$ [mm^2]	39.0	19.9	39.0	39.0	39.0
Deposition rate, R_{dep} [mm^3/s]	187.3	112.2	224.4	224.4	224.4
Volume of layer at traverse rate, R_{layer} [mm^3/s]	107.3	67.4	82.7	132.2	99.1
Fill ratio, R_{dep}/R_{layer}	1.7	1.7	2.7	1.7	2.3

Table 5 Baseline results of Vickers hardness testing, HV0.2, performed on the as-received materials

	Substrate plate 6061-T651	Filler 6061-T6
Average	104.6	105.2
Standard deviation	2.8	2.5
Maximum	109.0	110.0
Minimum	101.0	101.0
No. of tests	25	25

samples, which were 89.4 mm long, 19.05 mm wide, and 6.35 mm thick. The samples were oriented perpendicular to the grooves such that the gauge length was centered on the AFSD repairs. The thickness of the samples, 6.35 mm, corresponds to the depth of the repaired grooves as illustrated in the figure. Individual samples were designated by the groove geometry (V, R, or S), the test type (T = tensile, F = fatigue), and a sample number (i.e., the designation RF1 refers to the 1st fatigue sample from the R groove).

3 Results

3.1 Metallography and microhardness testing

The microstructure of the as-received substrate was documented as a baseline for comparison to the AFSD material. Figure 5 shows the microstructure of the 6061-T651 plate to contain transversely elongated grains associated with deformation during rolling, with grain sizes ranging from approximately 5 μm in the through-thickness direction to 25 μm in the in-plane direction of the plate. The microstructure is typical of a 6061 alloy in the -T6 or -T651 condition [30, 31], containing finely distributed particles of excess Mg_2Si

decorating the grain boundaries and interiors [23, 30, 32], and coarser (typically >1 μm) Fe-containing intermetallic particles [26, 30, 33].

Figure 6 shows cross sections of the three grooves after filling by AFSD. In all three images, the microstructure is well stirred down to a depth of 3.1–3.5 mm below the surface, which has been machined to be coplanar with the original substrate surface. The visible asymmetry in the stirred material is related to the relative directions of rotation and translation of the tool. In AFSD, one side of the tool is rotating toward the translation direction (called the "advancing" side) and the other is rotating away from the translation direction (called the "retreating" side), and the difference causes the fill material to penetrate more deeply on the advancing side [34, 35]. This can be seen in Fig. 6, where the advancing side in the original fill pass was on the left side in the images. Consideration of the relative sizes of the 9.4-mm filler metal and the 38-mm tool head reveals that the width of the stirred zone is associated with the diameter of the tool rather than that of the filler material.

The stir zone is one of four distinct microstructures associated with friction stir processes, and observed in the samples: stir zone (SZ), thermomechanical affected zone (TMAZ), heat-affected zone (HAZ), and base metal (BM) [26, 36]. The SZ comprises heavily deformed filler metal that was deposited during the process. It often has a striated morphology associated with material flow, and refined, equiaxed grains resulting from dynamic recrystallization [22, 26]. The TMAZ refers to regions where the heated substrate material has been plastically deformed by the shear forces transferred from the rotating feedstock, but without sufficient flow to achieve physical mixing with the deposited feedstock material. Thus, the TMAZ occurs between the stir zone and the HAZ, with typical characteristics including material flow, breakup of inclusions, and distortion of interfaces or boundaries. The depth and lateral extent of the TMAZ depend upon the relative stiffness of the heated feedstock and substrate, and

Table 6 Tabulated results of tensile testing samples from the AFSD-filled V, R, and S grooves in the 6061 substrate

Sample ID	Young's modulus, GPa	Yield strength, MPa	Yield strength, %	Tensile strength, MPa	Tensile strength, %	Elongation at fracture, %
VT1	67.8	90.3	37.6	153.2	52.8	10.5
VT2	48.8	97.2	40.5	175.6	60.5	10.9
VT3	58.5	108.0	45.0	173.0	59.7	10.2
VT4	44.8	106.5	44.4	162.7	56.1	10.0
RT1	64.3	87.2	36.3	155.4	53.6	10.5
ST1	55.9	88.9	37.0	124.3	42.9	6.6
ST2	77.9	90.3	37.6	152.4	52.5	8.5
ST3	53.9	93.4	38.9	140.4	48.4	7.7
ST4	87.4	102.1	42.5	169.5	58.5	9.4

Table 7 Summarized results of fatigue testing from the AFSD-filled R and V grooves, and predicted stress amplitude for 6061-T6 at the measured cycles to failure (based on [39])

Sample ID	Applied stress amplitude $\pm\sigma_a$, MPa	Cycles to failure, $N_f \times 10^5$	Predicted stress amplitude [40] $\pm\sigma_p$, MPa	Ratio σ_a/σ_p, %
RF1	61.3	1.23	137.8	44.5
RF2		1.30	136.7	44.9
RF3		2.40	126.1	48.6
RF4		3.80	120.0	51.1
RF5		9.33	111.5	55.0
RF6		>10.0	<111.0	>55.2
VF3	70.5	0.011	539.1	13.1
VF2		0.21	197.4	35.7
VF1		0.22	194.3	36.3

on the groove and feedstock geometry. The HAZ is similar to that of a welding process, but is typically smaller and less pronounced due to the relatively low temperature of the AFSD process. These microstructures are labelled 1–4 in Fig. 6 c, and are shown in more detail in Fig. 7. In comparison to Fig. 5 b, there are notable similarities to the T-651 microstructure, including high concentrations of submicron Mg_2Si precipitates with larger, interspersed Fe-containing intermetallics. The images show a range of concentrations for the Mg_2Si particles, ranging from a high in parts of the TMAZ (Fig. 7b) to a low in the HAZ (Fig. 7c). In addition, the tendency for these precipitates to decorate the grain boundaries is generally suppressed in the SZ, TMAZ, and HAZ (Fig. 7a–c) relative to the underlying substrate (Figs. 4b and 7d). These differences arise from the competing mechanisms of dissolution of the intermetallic particles during heating, and re-precipitation during cooling, with the (localized) final result dependent upon maximum temperature reached during the process, as well as the associated heating and cooling rates.

Higher magnification images of the three groove geometries are shown in Fig. 8. The images reveal all three grooves to have been filled, but with incomplete bonding in the lower third of the grooves. This is consistent with the results reported by Griffiths et al., where poor repair quality was observed at depths exceeding ~1.7 mm during groove and hole filling in 7075 aluminum [22]. In the bottom 1.5 mm of the V groove shown in Fig. 8 a, the interface between the substrate and the filler metal is nearly undistorted and exhibits open gaps on both sides (arrows). This indicates a lack of deformation of
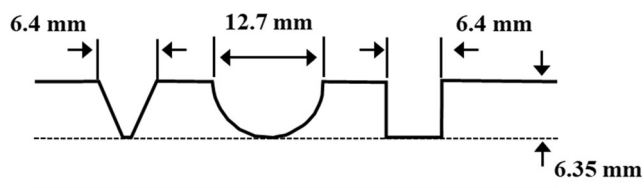
the substrate at that depth, and a resultant lack of mixing and/or bonding at the interface. In between the top of the unbonded interface and the top of the image, the microstructure exhibits increasingly severe deformation, with concurrent distortion of the original V groove geometry. In the upper-right portion of the groove, the interface exhibits a jagged pattern characteristic of mixing at a temperature below the welding temperature [37]. That section of the interface exhibits partial bonding with entrained oxide inclusions and porosity up to approximately 0.75 mm from the top of the image. Closer to the top of the image, the microstructure is fully stirred, as evidenced by the absence of any residual indication of the original groove location or geometry.

Figure 8 b and c show a similar extent of unbonded interface in the R and S groove geometries, respectively, with the unbonded interfaces again indicated by arrows. Above that, the interfaces again show the characteristic jagged appearance at the right-hand side of the images, and complete mixing near the top. At the left side of Fig. 8 b, the interface is unmixed, as evidenced by the abrupt change in microstructure across the groove boundary, but void-free and apparently in good contact. In Fig. 8 c, the S groove geometry shows good mixing at the left-hand side, where there is no remaining evidence of the original groove wall, but retained unbonded interfaces along the bottom and right side of the groove. Inside the groove itself, there is a visible boundary between two different microstructures that can be identified as striated filler metal (right side) and highly deformed substrate material that has been forced into the groove (as evidenced by the pronounced flow lines). A proposed mechanism for this type of morphology suggests that tool forces cause fracture or collapse of the groove wall [22]. Note that the V and R groove images both show evidence of voids or cracks in the filler metal inside of the grooves.

Hardness depth profiles were performed at the locations indicated in Fig. 6. For reference, the measured microhardnesses for the as-received substrate and filler are provided in Table 5. The average hardness in the as-received plate and feedstock, 105 HV0.2, is consistent with the reported hardness for -T651

Fig. 2 Geometry of the grooves machined into the substrate plates to simulate material removal during a repair operation

Fig. 3 AFSD build on the 6061-T651 plate (450 mm × 305 mm). The depositions cover, from left, V grooves, R grooves, S grooves, and an additional section not used in this investigation
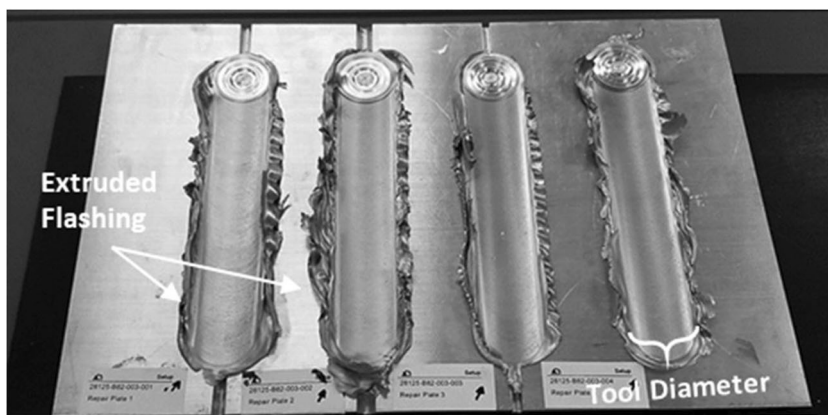
provided in Table 2, 107 HV. Figure 9 a–c show that the combination of thermal and mechanical conditions during the AFSD process decreases the hardness of both the substrate and filler alloys to the range of 45–75 HV0.2. The hardness profiles are uniform across the different test locations and sample geometries, starting at 70–75 HV0.2 near the surface, decreasing to 45–50 HV0.2 at the base of the groove, and then increasing with increasing depth below the repair. As shown in Fig. 9 b, even as the depth approaches the back surface of the substrate, the hardness regains only 71% of the initial value of 105 HV0.2. This again indicates the depth of the thermal affects in the substrate below the repair.

3.2 Tensile testing

The results of tensile testing are summarized in Table 6, where the measured yield and tensile strengths are also provided as a percentage of the specification for 6061-T651 [27]. The measured Young's moduli range from 44.8 to 87.4 GPa, with no correlation to the groove geometry. For reference, these values can be compared to the published value of 68.9 GPa [38]. The measured yield strengths range from 87.2 to 108.0 MPa, or 36 to 45% of the specified yield strength for 6061-T651, and the measured tensile strengths range from 124.3 to 175.6 MPa, or 43 to 61% of the specified value.

Figure 10 shows the stress versus strain curves from the tensile testing, segregated by groove geometry. The V groove results in Fig. 10 a exhibit typical behavior for a ductile material, with a poorly defined elastic region, no distinct yield point, and strain hardening prior to reaching the ultimate stress. The perturbation at ~2% strain indicates the point at which the tests were interrupted to remove the extensometer. There is some scatter in the ultimate stress levels, but in general the curves are consistent. In contrast, the S groove results in Fig. 10 c show significantly more scatter in both the ultimate stress and the elongation to failure. This suggests less consistency in the ASFD filling process with the S groove geometry. Finally, the single R groove result in Fig. 10 b is generally consistent with the V groove results up to a peak stress of 155 MPa, at which point the data exhibit evidence of

Fig. 4 Showing the geometry of the mechanical test samples: **a** tensile and **b** fatigue. All samples were 6.35 mm thick, and all dimensions shown are in millimeters
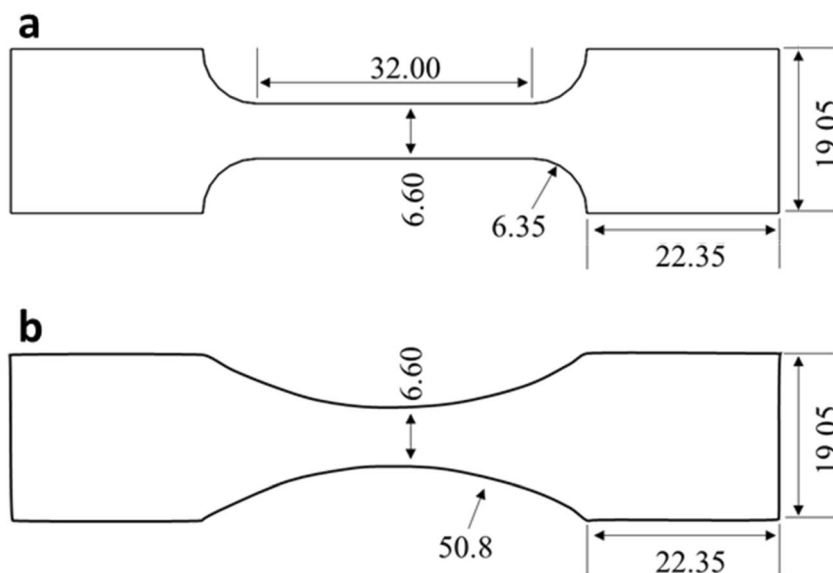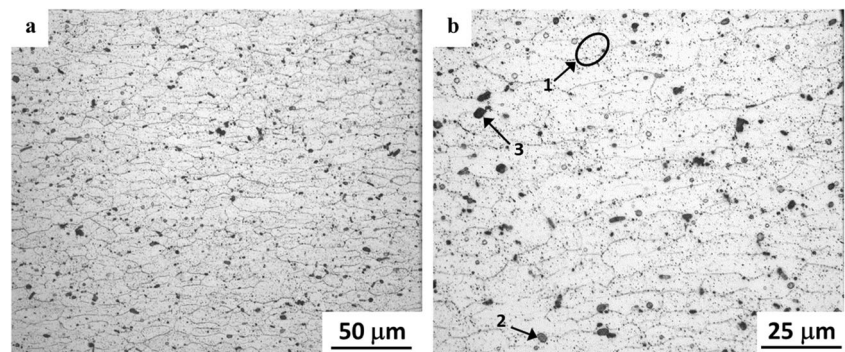
Fig. 5 Light optical microscopy images showing the as-received microstructure in the 6061-T651 substrate. The annotations in (**b**) indicate examples of (1) excess Mg$_2$Si inclusions, (2) Fe-containing intermetallic inclusions, and (3) etch pits

a premature partial failure. This discontinuity is pronounced in the R groove sample; however, close inspection of the balance of the data reveals evidence of similar, less pronounced features in other samples, including ST1, ST2, ST3, and VT3. The observed behavior was attributed to early failure of weakly bonded regions of the filler-substrate interface, which was further assessed by fractography.
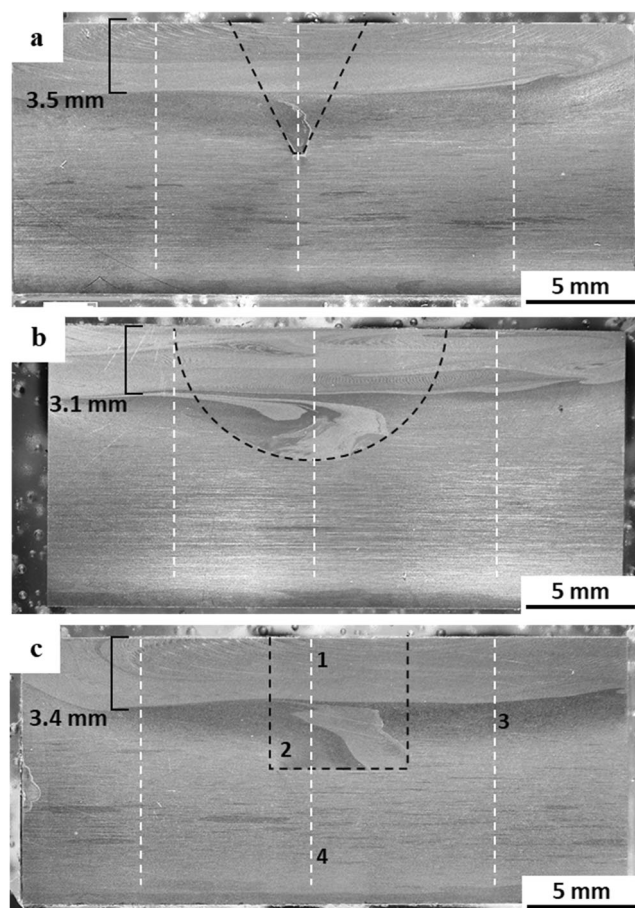
Fig. 6 Light optical microscopy images of cross sections from the three AFSD-filled grooves in the 6061-T651 plate: **a** V groove, **b** R groove, and **c** S groove. The microstructures shown in Fig. 7 were observed at the locations indicated in (**c**): (1) SZ, (2) TMAZ, (3) HAZ, and (4) BM. The vertical lines indicate the locations of the hardness profiles in Fig. 9

Figure 11 shows the profile of the fracture in tensile sample RT1, along with the associated fracture surfaces. The images are oriented such that the stir zone was on the top edge of the samples, and the base of the groove was approximately even with the bottom edge. The shape of the bottom half of the fracture profile in Fig. 11 a and b closely resembles the cross section of the filled R groove shown in Fig. 8 b, and suggests that the failure involved pullout of the filler alloy along that section of the filler-substrate interface. However, by overlaying the images, it was possible to ascertain that the interface actually aligns with the jagged crack to the right of the fracture in Fig. 11 b, and that the end of the pullout approximately aligns with the internal defect indicated by the dashed line in Fig. 8 b. The unbonded filler-substrate interface noted in Fig. 8 b is visible as a gap at the bottom of Fig. 11 c and d, and is labelled "iv" in Fig. 11 d. In the top half of the sample, the fracture surface exhibits a smooth appearance and a 45° orientation characteristic of a shear lip formed during ductile tensile overload, labelled "i" in Fig. 11 b–d. In between the shear lip and the underlying pullout, there is an extended, axially oriented planar surface that aligns with bottom of the stir zone. That surface, labelled "ii" in Fig. 11 c and d, shows a striated texture consistent with the AFSD tool motion, and indicating incomplete bonding.

Figure 12 provides a similar analysis of the fracture from the highest tensile strength sample VT2. Figure 12 a and b show the fracture profile, emphasizing the thin ligament of substrate alloy that extended below the base of the V groove, and the presence of unbonded interfaces in the bottom ~1.5 mm of the groove. In particular, Fig. 12 b shows unbonded interfaces on both sides of the V-shaped filler alloy, again suggesting the interfacial pullout mechanism discussed above. In this case, the unbonded surfaces show periodic striations that are residual from the motion of the AFSD tool, but no evidence of macroscopic shear deformation. In addition to the unbonded surface at the bottom of the groove, Fig. 12 c and d show the fracture surfaces to exhibit ductile morphology in the SZ near the top of the sample, and a layered morphology in the mid-section. Figure 13 shows SEM micrographs from the two locations designated "i" and "ii" in Fig. 12 d. Figure 13 a shows the surface from the layered mid-section

Fig. 7 Light optical micrographs of the microstructures observed at locations 1–4 in Fig. 6 c: **a** stir zone (SZ) at location 1, **b** thermomechanical affected zone (TMAZ) at location 2, **c** heat-affected zone (HAZ) at location 3, and **d** base metal (BM) at location 4
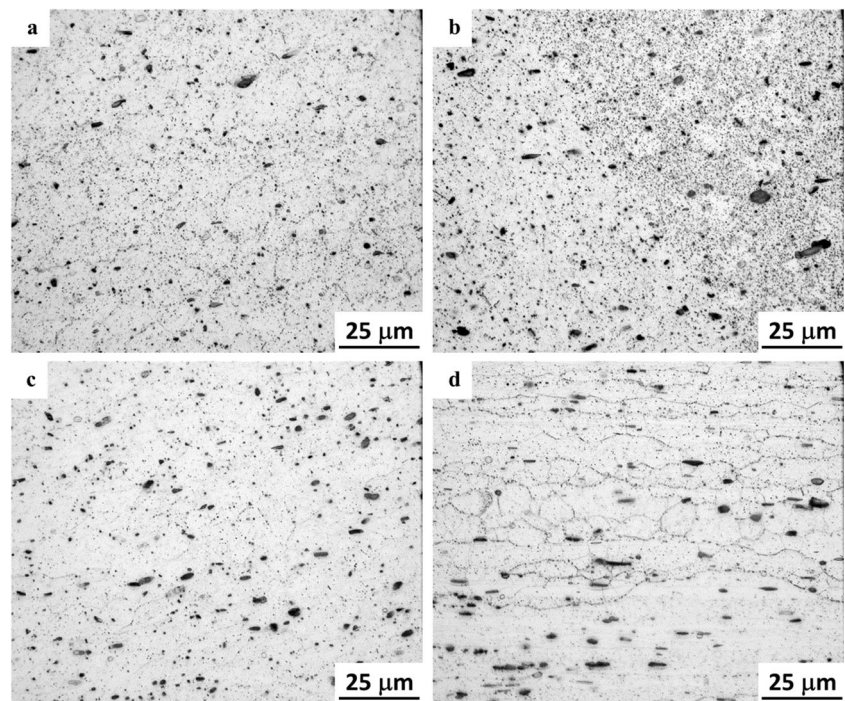
to exhibit mixed mode fracture, with intergranular cleavage and pullouts interspersed with dimpling characteristic of ductile overload, while Fig. 13 b shows the surface from the base of the groove to be heavily oxidized, with no evidence of ductile fracture. Given the previous observations of poor interfacial bonding at the base of the grooves, the conclusion can be drawn that the portion of the fracture surface labelled "ii" in Fig. 12 d was a preexisting surface that was not bonded during the AFSD process.

3.3 Fatigue testing

The R and V groove geometries were selected for fatigue testing based on the metallographic observations and the tensile results. The limited number of specimens precluded construction of full S-N curves, so all tests were performed at a stress amplitude, σ_a, equal to 70% of the average measured yield strength, σ_{YS}, reported in Table 6 for the two groove geometries. The testing utilized a fully reversed ($R = -1$) stress cycle under load control, and the individual tests were run to failure or to one million ($N = 10^6$) cycles, whichever occurred first.

Results from the fatigue testing are summarized in Table 7. The R groove geometry performs better than the V groove under the given test conditions; however, due to the difference in measured yield strengths, the fatigue tests were performed at different stress amplitudes, 61.3 versus 70.5 MPa. Additionally, because the number of tensile samples was small, particularly for the R groove geometry, the relative stress ratios (σ_a / σ_{YS}) may not be accurate. As a result, caution

should be used when comparing the cycles to failure between the different geometries.

Figure 14 presents the fracture surfaces from the R groove samples exhibiting the highest and lowest cycles to failure, N_f (excluding the sample that was terminated prior to failure). In the images, the top edge of the sample corresponds to the top of the filler material, while the bottom edge is at the approximate bottom of the groove. The images show the surfaces from samples RF5 and RF1, which failed at 9.33×10^5 and 1.23×10^5 cycles, respectively. Both surfaces show a thin ligament of fractured substrate alloy near the bottom of the image, one or more fatigue initiation sites indicated by the arrows, and typical flat fatigue fractures extending to pronounced shear lips in approximately the top third of the samples. The initiation sites are at the bottom of the filled groove, and at the approximate axial location indicated by the dashed line in Fig. 8 b.

4 Discussion

Remanufacturing is an approach to improve sustainability by restoring worn or damaged components to the original condition. A common remanufacturing approach is to repair surfaces that have been worn, cracked, or corroded by mechanically removing the damaged material, and using an additive material technology to rebuild the surface. Because the repairs must perform as well or better than the original design, it is critical to understand how the strengths and limitations of the additive process can be leveraged to optimize the mechanical
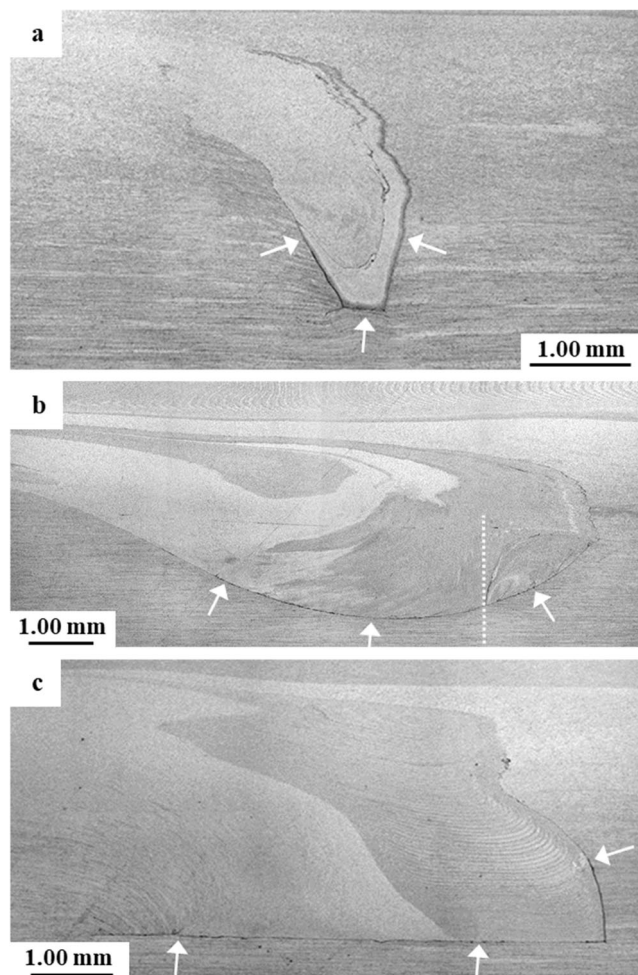
Fig. 8 Light optical microscopy images of cross sections from the three AFSD-filled grooves in the 6061-T651 substrate: **a** V groove, **b** R groove, and **c** S groove. The dashed line in (**b**) indicates the approximate position of the fracture surfaces in Fig. 13 a and b

Fig. 9 Vickers hardness depth profiles for the AFSD-filled grooves: **a** V groove, **b** R groove, and **c** S groove. Note the different scale for the x-axis in (**b**)

performance of the repair material. As stated in the introduction, AFSD is a recently developed additive methodology that combines the microstructural refinement known to occur in FSW with the capability to add new material. The potential to apply AFSD as a repair technology is enticing because it is a solid-state process that can create highly refined microstructures with isotropic properties, and without many of the challenges associated with fusion processes. However, most of the published literature addresses AFSD within the context of manufacturing or surface cladding. Thus, there exists a need to further explore the benefits and limitations of the technology as applied to volumetric surface repairs in a variety of materials.

The repair geometries evaluated in this work were intended to simulate the process described above, whereby a groove has been machined into the surface to remove damaged material. The three groove geometries depicted in Fig. 2 were evaluated for the effectiveness of the AFSD repair. The process parameters used to apply the AFSD material (Table 3) were consistent with prior reports [22, 32], but were modified to account for the repair
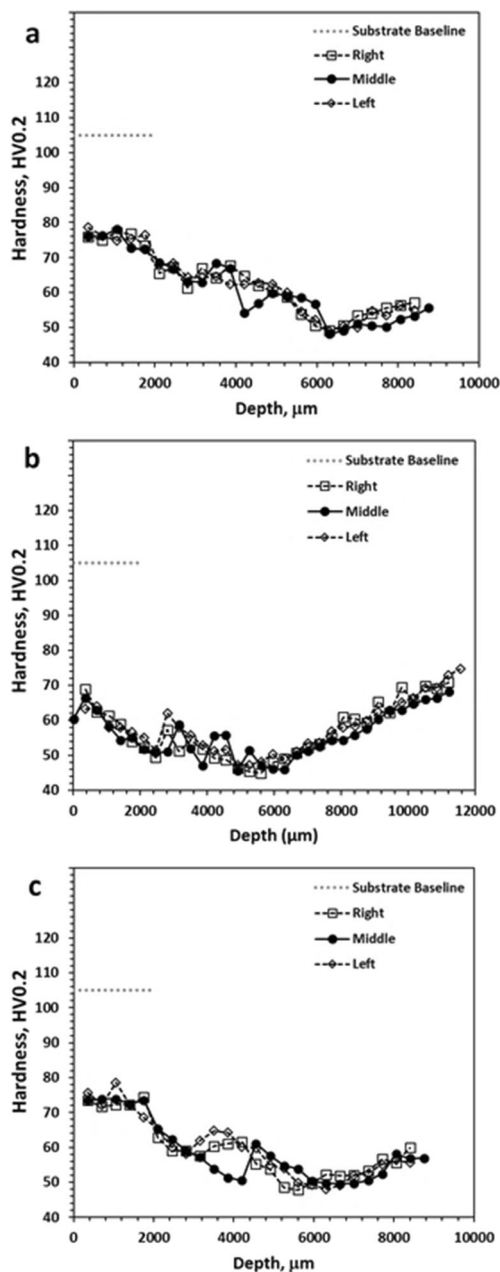
geometry. Aspects of the AFSD that were not optimized for the experiment are the relative dimensions of the groove and filler material, and the design of the tool head. There is some published evidence that optimization of these relative dimensions could have a significant impact on the depth of effective bonding between the filler and the substrate [22].

The lack of deformation at the base of the grooves indicates that, below a certain depth, the conditions during the deposition were not conducive to effective bonding due to insufficient shear. For the current tool/groove geometries and
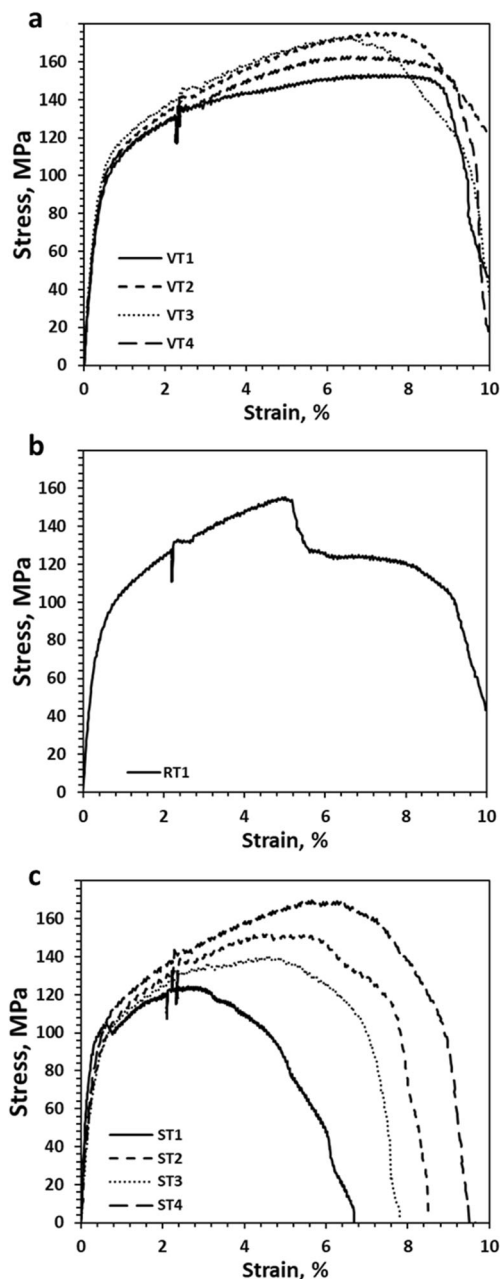
Fig. 10 Stress-strain curves from tensile testing of the different groove geometries: **a** V groove, **b** R groove, and **c** S groove

process conditions, the effective repair depths were limited to approximately 3.1–3.5 mm in the 6061-T651 substrate. In addition, the Vickers hardness of the deposited 6061 shows a significant decrease of over 30% near the surface of the repairs, with even larger decreases in the underlying material. This is attributable to dissolution of the "β" hardening phase, which has been documented in the SZ during FSW and AFSD [32, 41]. The measured hardness values in the SZ, 50-75 HV0.2, are consistent with results from a prior investigation of AFSD 6061, 55–73 HV [32], and the fact that the original baseline hardness is not recovered below the repair indicates that the substrate also loses temper as a result of the applied

thermal exposure. The hardness data therefore indicate that the 6061 AFSD filler is under-matched (weaker) relative to both the as-received 6061-T651 plate and the 6061-T6 feedstock. Furthermore, the HAZ introduces an accompanying under-matched zone in the substrate beneath the AFSD feature.

The metallography and fractography supported the presence of complete disbonds near the bottom of the grooves, with partial bonding possible at intermediate depths. As a result, the strengths reported in Table 6 may not be representative of the deposited alloy because the effectively-bonded cross sections are actually smaller than full cross section of the tensile samples. From the discussion of Fig. 8, where it was estimated that the bottom ~1.5 mm of the grooves exhibited open gaps at the interfaces, there is a likelihood that approximately 25% of the cross section of the 6.35-mm-thick tensile samples is either unbonded or only weakly bonded. This observation can be used to provide an approximate correction to the cross-sectional area for the purpose of estimating the actual strength of the AFSD 6061 alloy from the strengths reported in Table 6. The resultant corrected average yield and tensile strengths, 128 and 208 MPa, are 53% and 72% of the -T651 specification given in Table 2, respectively. Similarly, the corrected values correspond to 116% and 102%, respectively, of the specification for 6061-T4 (naturally aged), and 151% and 139%, respectively, of the specifications for 6061-O (fully annealed). The tensile data thus suggest that the average condition of the deposited alloy most closely resembles the -T4 temper. This is consistent with the findings from Vickers hardness testing, where the deposited 6061 exhibited hardness values in the range of 50–75 HV0.2, while Table 2 indicates a target value of 74 HV0.2 for 6061-T4. For comparison, relevant fabrication/welding codes provide a benchmark for the HAZ-induced strength reduction that can occur during fusion (welding) processes. AWS D1.2 specifies a strength reduction of 40% associated with the HAZ formed during metal inert gas (MIG) welding of 6061, or a minimum retained strength of 165 MPa [40]. In addition, published data indicate comparable strength levels in tungsten inert gas (TIG) welded 6061, 169–174 MPa [42].Thus, the results indicate AFSD provides some improvement in strength relative to "acceptable" strength levels associated with relevant fusion processes, such as MIG and TIG welding.

The fatigue life in the repaired R grooves ranged from $<1.25\times10^5$ to $>1.0\times10^6$ cycles at the applied stress amplitude of 61.3 MPa. For comparison, data from fully reversed ($R = -1$) fatigue testing of 6061-T6 has been reported to follow the relation [39]

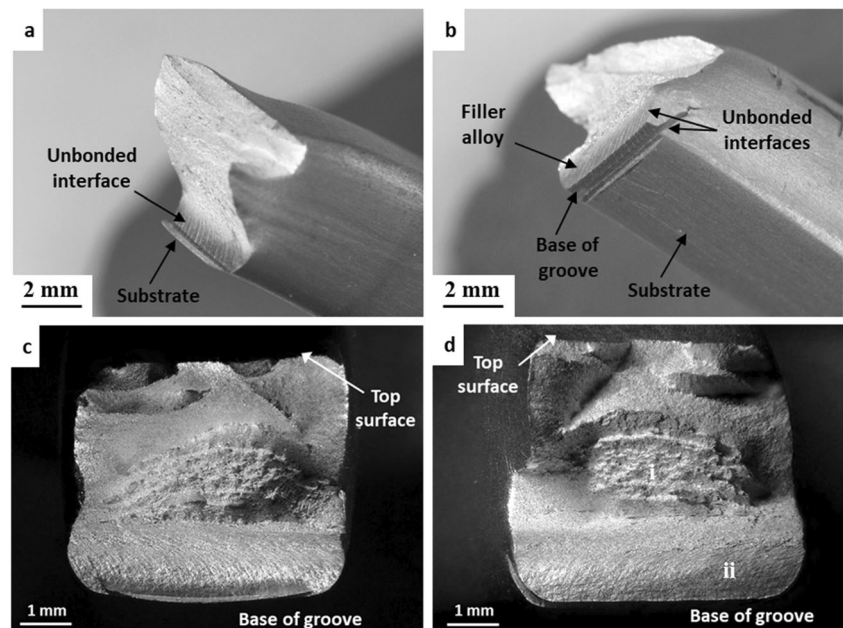$$\sigma_a = \frac{14479}{\sqrt{N_f}} + 96.5 \ [MPa] \tag{4}$$

where N_f refers to the average cycles to failure. The predicted stress amplitude, σ_p, provided in Table 7, refers to the value of σ_a calculated for the 6061-T6 base metal by substituting the measured cycles to failure into Eq. (4). The calculated values

Fig. 11 Light optical microscope images: **a**, **b** the profile of the fracture from tensile sample RT1 and **c**, **d** the corresponding fracture surfaces from the same sample. The labelled features are (i) ductile shear lip, (ii) weakly bonded interface at the base of the SZ, (iii) unbonded surface from near the base of the groove, and (iv) unbonded filler-substrate interface
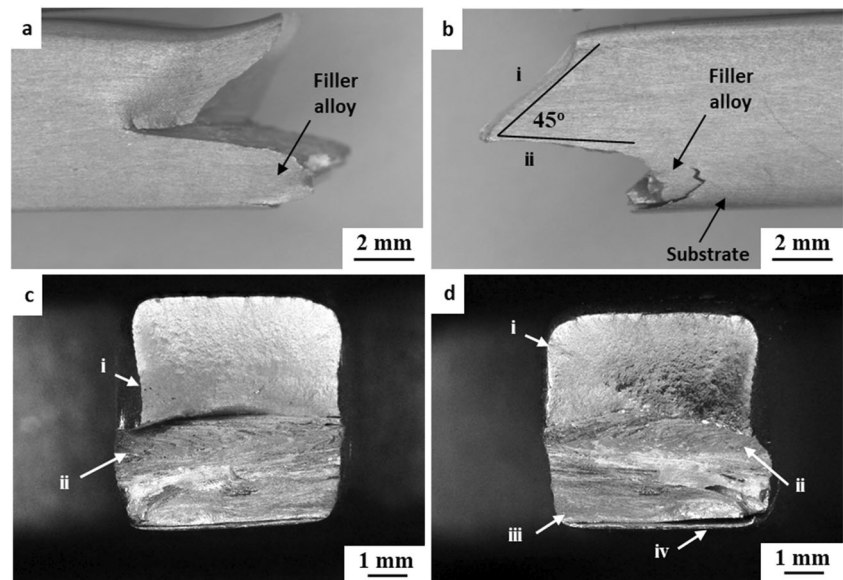
of σ_p for the -T6 temper may not be directly relevant to the AFSD material due to the loss of temper evidenced by the hardness and tensile strength discussed above, but they are provided here as a point of reference. From Table 7, the σ_a of the AFSD-filled R groove samples is approximately 50% of σ_p at comparable N_f. This is generally consistent with at least one published report for AFSD of AA2219 [4], and multiple investigations of fatigue in FSW of aluminum alloys have reported that the performance can range from ~50 to >100% of the base metal, depending on the FSW process parameters and fatigue test conditions [43, 44]. Thus, the observed performance appears to be within the range of prior relevant observations, with potential improvements available by optimization of process parameters.

5 Conclusions

Additive friction stir deposition of aluminum alloy 6061 was investigated as a means to fill machined grooves in substrate plates of rolled aluminum alloy 6061-T651. The groove geometries were intended to simulate a repair in which damaged material is mechanically removed and replaced using an additive process. This process is widely used in remanufacturing processes, and application to aluminum alloys is critical to lifetime extension in the automotive, aerospace, and defense industries. Three groove geometries were evaluated based upon metallographic inspection, and tensile and fatigue testing. The results indicate that, for the process conditions and tool/groove geometries used in this study, effective mixing was

Fig. 12 Light optical microscope images of **a**, **b** the profile of the fracture from tensile sample VT2 and **c**, **d** the corresponding fracture surfaces from the same sample. Scanning electron micrographs from the labelled locations (i) and (ii) in (**d**) are shown in Fig. 13

Fig. 13 Scanning electron micrographs from the labelled locations in Fig. 12 d: **a** location "i" from the ductile SZ and **b** location "ii" from the unbonded base of the groove
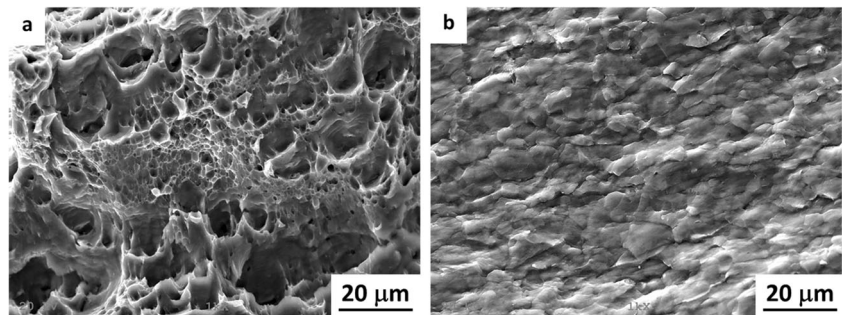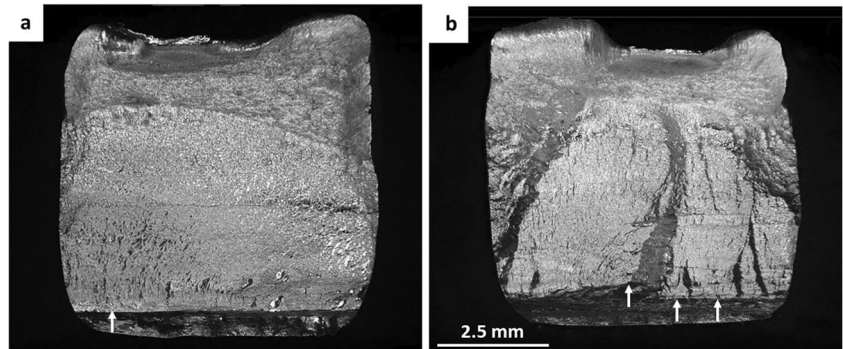

Fig. 14 Fracture surfaces from fatigue samples **a** RF5 and **b** RF1. The scalebar in (**b**) also applies to (**a**)

achieved to a depth of more than 3 mm. In that part of the material, the process effectively eliminated the groove boundary, leaving well-mixed material with no clear differentiation between the filler and substrate materials. Below that depth, however, the groove geometry is still evident, and the interface between the filler and substrate materials exhibits poor bonding associated with insufficient shear deformation. This suggests that the practical limitation on groove depth that can be filled using the current tool geometry, material combination, and processes conditions is likely to be ~3 mm.

The thermomechanical process experienced by the 6061-T6 filler alloy during the AFSD effectively erased the artificial age hardening associated with the -T6 specification, and left the filler alloy in what was equivalent to the naturally aged -T4 condition. Microhardness depth profiling indicated a similar condition in the 6061 substrate below, and adjacent to, the AFSD repair. Tensile testing indicated that the ultimate strength of the deposited alloy, 208 MPa, exceeded code requirements (173 MPa) and published results (169–174 MPa) for fusion-welded 6061-T6. These results indicate that solid-state repairs enabled by AFSD have the potential to provide improved mechanical properties relative to fusion-based processes.

6 Future work

The results of this investigation indicate several opportunities to optimize the AFSD process through continued development. The limitations of the method that were identified here

(the depth of effective mixing and the loss of temper in precipitation hardened alloy) may be mitigated with further optimization of tool and groove geometry, process parameters, and selection of filler material to match substrate properties.

Declarations

Ethics approval Not applicable.

Consent to participate Not applicable.

Consent for publication Not applicable.

Conflict of interest The authors declare no competing interests.

References

1. Li L, Liu Z, Snow M (2006) Effect of defects on fatigue strength of GTAW repaired cast aluminum alloy. WELDING JOURNAL-NEW YORK 85(11):264

2. Shankar K, Wu W (2002) Effect of welding and weld repair on crack propagation behaviour in aluminium alloy 5083 plates. Materials & design 23(2):201–208

3. Qi S, Wen Q, Ji S, Meng X, Wu B, Qi W (2019) New technique of radial-additive friction stir repairing for exceeded tolerance holes. The International Journal of Advanced Manufacturing Technology 105(11):4761–4771

4. Anderson-Wedge K, Avery DZ, Daniewicz SR, Sowards JW, Allison PG, Jordon JB, Amaro RL (2021) Characterization of the fatigue behavior of additive friction stir-deposition AA2219. International Journal of Fatigue 142:105951

5. Heidarzadeh A, Mironov S, Kaibyshev R, Çam G, Simar A, Gerlich A, Khodabakhshi F, Mostafaei A, Field DP, Robson JD, Deschamps A (2020) Friction stir welding/processing of metals and alloys: a comprehensive review on microstructural evolution. Progress in Materials Science:100752.

6. Liu FC, Hovanski Y, Miles MP, Sorensen CD, Nelson TW (2018) A review of friction stir welding of steels: Tool, material flow, microstructure, and properties. Journal of Materials Science & Technology 34(1):39–57

7. Khodabakhshi F, Gerlich AP (2018) Potentials and strategies of solid-state additive friction-stir manufacturing technology: a critical review. Journal of Manufacturing Processes 36:77–92

8. Palanivel S, Mishra RS (2017) Building without melting: a short review of friction-based additive manufacturing techniques. International Journal of Additive and Subtractive Materials Manufacturing 1(1):82–103

9. Srivastava M, Rathee S, Maheshwari S, Noor Siddiquee A, Kundra TK (2019) A review on recent progress in solid state friction based metal additive manufacturing: friction stir additive techniques. Critical Reviews in Solid State and Materials Sciences 44(5):345–377

10. Rivera OG, Allison PG, Brewer LN, Rodriguez OL, Jordon JB, Liu T, Whittington WR, Martens RL, McClelland Z, Mason CJ, Garcia L (2018) Influence of texture and grain refinement on the mechanical behavior of AA2219 fabricated by high shear solid state material deposition. Materials Science and Engineering: A 724:547–558

11. Hang ZY, Jones ME, Brady GW, Griffiths RJ, Garcia D, Rauch HA, Cox CD, Hardwick N (2018) Non-beam-based metal additive manufacturing enabled by additive friction stir deposition. Scripta Materialia 153:122–130

12. Avery DZ, Rivera OG, Mason CJ, Phillips BJ, Jordon JB, Su J, Hardwick N, Allison PG (2018) Fatigue behavior of solid-state additive manufactured inconel 625. JOM 70(11):2475–2484

13. Griffiths RJ, Perry ME, Sietins JM, Zhu Y, Hardwick N, Cox CD, Rauch HA, Hang ZY (2019) A perspective on solid-state additive manufacturing of aluminum matrix composites using MELD. Journal of Materials Engineering and Performance 28(2):648–656

14. Schultz JP, Creehan KD (2017) Fabrication tools for exerting normal forces on feedstock US Patent 9205578 B2.

15. Gerlich AP (2017) Critical assessment 25: friction stir processing, potential and problems. Materials Science and Technology 33(10):1139–1144

16. Chen YC, Fujii H, Tsumura T, Kitagawa Y, Nakata K, Ikeuchi K, Matsubayashi K, Michishita Y, Fujiya Y, Katoh J (2009) Friction stir processing of 316L stainless steel plate. Science and Technology of Welding and Joining 14(3):197–201

17. Kandasamy K, Renaghan LE, Calvert JR, Creehan KD, Schultz JP (2013) Solid-state additive manufacturing of aluminum and magnesium alloys. Proceedings of materials science and technology, Montreal, pp 59–69

18. Gray DT (2009) Modeling and characterization of friction stir fabricated coatings on Al6061 and Al5083 substrates. Dissertation, Virginia Polytechnic Institute and State University

19. Rivera OG, Allison PG, Jordon JB, Rodriguez OL, Brewer LN, McClelland Z, Whittington WR, Francis D, Su J, Martens RL, Hardwick N (2017) Microstructures and mechanical behavior of Inconel 625 fabricated by solid-state additive manufacturing. Materials Science and Engineering: A 694:1–9

20. MELD Brochure – MELD Manufacturing Corporation. http://meldmanufacturing.com/technology-overview/

21. Priedeman JL, Phillips BJ, Lopez JJ, Tucker Roper BE, Hornbuckle BC, Darling KA, Jordon JB, Allison PG, Thompson GB (2020) Microstructure development in additive friction stir-deposited Cu. Metals 10(11):1538

22. Griffiths RJ, Petersen DT, Garcia D, Yu HZ (2019) Additive friction stir-enabled solid-state additive manufacturing for the repair of 7075 aluminum alloy. Applied Sciences 9(17):3486

23. Ozturk F, Sisman A, Toros S, Kilic S, Picu RC (2010) Influence of aging treatment on mechanical properties of 6061 aluminum alloy. Materials & Design 31(2):972–975

24. Buha J, Lumley RN, Crosky AG (2006) Microstructural development and mechanical properties of interrupted aged Al-Mg-Si-Cu alloy. Metallurgical and Materials Transactions A 37(10):3119–3130

25. Edwards GA, Stiller K, Dunlop GL, Couper MJ (1998) The precipitation sequence in Al–Mg–Si alloys. Acta Materialia 46(11):3893–3904

26. Rutherford BA, Avery DZ, Phillips BJ, Rao HM, Doherty KJ, Allison PG, Brewer LN, Jordon JB (2020) Effect of thermomechanical processing on fatigue behavior in solid-state additive manufacturing of Al-Mg-Si Alloy. Metals 10(7):947

27. ASTM B209M-14 (2014) Standard specification for aluminum and aluminum-alloy sheet and plate. ASTM International, West Conshohocken

28. ASTM B557-15 (2015) Standard test methods for tension testing wrought and cast aluminum- and magnesium-alloy products. ASTM International, West Conshohocken

29. ASTM E466-15 (2015) Standard practice for conducting force controlled constant amplitude axial fatigue tests of metallic materials. ASTM International, West Conshohocken

30. María Abreu Fernández C, Rey RA, Julia Cristóbal Ortega M, Verdera D, Vidal CL (2018) Friction stir processing strategies to develop a surface composite layer on AA6061-T6. Materials and Manufacturing Processes 33(10):1133–1140

31. Rajaa SM, Abdulhadi HA, Jabur KS, Mohammed GR (2018) Aging time effects on the mechanical properties of Al 6061-T6 alloy. Engineering, Technology & Applied Science Research 8(4):3113–3115

32. Phillips BJ, Avery DZ, Liu T, Rodriguez OL, Mason CJ, Jordon JB, Brewer LN, Allison PG (2019) Microstructure-deformation relationship of additive friction stir-deposition Al–Mg–Si. Materialia 7:100387

33. Aluminum Association (1984) Aluminum: properties and physical metallurgy. John E. Hatch, ed. ASM International

34. Perry ME, Griffiths RJ, Garcia D, Sietins JM, Zhu Y, Hang ZY (2020) Morphological and microstructural investigation of the non-planar interface formed in solid-state metal additive manufacturing by additive friction stir deposition. Additive Manufacturing 35:101293

35. Mishra RS, Ma ZY (2005) Friction stir welding and processing. Materials science and engineering: R 50(1-2):1–78

36. Çam G (2011) Friction stir welded structural materials: beyond Al-alloys. International Materials Reviews 56(1):1–48

37. Ozan S (2020) Effect of friction stir welding on the microstructure and mechanical properties of AA 6063-T6 aluminum alloy. Materialwissenschaft und Werkstofftechnik 51(8):1100–1119

38. Handbook ASM (1990) Properties of wrought aluminum and aluminum alloys. ASM International Hand Book Volume 2:62–122

39. Yahr GT (1997) Fatigue design curves for 6061-T6 aluminum. Journal of Pressure Vessel Technology 119:211–215

40. AWS D1.2/D1.2M (2014) Structural welding code-aluminum. American Welding Society, Miami

41. Feng AH, Chen DL, Ma ZY (2010) Microstructure and low-cycle fatigue of a friction-stir-welded 6061 aluminum alloy. Metallurgical and Materials Transactions A 41(10):2626–2641

42. Lin H, Hwang JR, Fung CP (2016) Fatigue properties of 6061-T6 aluminum alloy butt joints processed by vacuum brazing and tungsten inert gas welding. Advances in Mechanical Engineering 8(4):1–13

43. de Oliveira Miranda AC, Gerlich A, Walbridge S (2015) Aluminum friction stir welds: Review of fatigue parameter data and probabilistic fracture mechanics analysis. Engineering Fracture Mechanics 147:243–260

44. Ranjan R, de Oliveira Miranda AC, Guo SH, Walbridge S, Gerlich A (2019) Fatigue analysis of friction stir welded butt joints under bending and tension load. Engineering Fracture Mechanics 206:34–45

Publisher's note Springer Nature remains neutral with regard to jurisdictional claims in published maps and institutional affiliations.